Modeling, Control and Experimental Evaluation of Multi-functional Converter System

Xiaokang Zhang, Jean-Yves Gauthier, Xuefang Lin-Shi, Romain Delpoux, Jean-François Trégouët

Modeling, Control and Experimental Evaluation of Multi-functional Converter System

Xiaokang Zhang, *Student Member, IEEE*, Jean-Yves Gauthier, Xuefang Lin-Shi, Romain Delpoux, and Jean-François Trégouët

***Abstract*—The multi-functional converter system (MFCS) is a special topology of three-phase AC motor drives, which inherently integrates a DC-voltage regulation function. Firstly, in order to explain the mechanism of the MFCS, an average model is derived. An equivalent circuit is developed, which explicitly reveals that the MFCS is equivalent to a cascaded DC/DC converter-DC motor drive system. Secondly, the inverter's mean duty-cycle is identified as an independent control degree of freedom for the DC-bus voltage. Then, the influence of pulse width modulation (PWM) on the DC-bus voltage is studied. It concludes that space vector PWM is invalid for the MFCS. To address this problem, the zero-sequence voltage injection PWM (ZSVIPWM) is proposed and actually sinusoidal PWM is a special case of the ZSVIPWM. Thirdly, an overall control strategy is proposed for the MFCS, which includes not only the vector control for the motor but also a closed-loop control for the DC-bus voltage. Finally, comparative experiments with the standard topology are carried out on a permanent magnet synchronous machine prototype to verify these theoretical analyses and the control strategy.**

***Index Terms*—Permanent magnet synchronous machine drives, DC/DC converter, neutral point, zero-sequence.**

NOMENCLATURE

DOF	Degree of freedom.
DCSUR	DC-source utilization ratio.
EVs, HEVs	Electric vehicles, hybrid electric vehicles.
EDC	Equivalent DC/DC converter.
FOC	Field oriented control.
FFT	Fast fourier transform.
MFCS	Multi-functional converter system.
PI	Proportional Integral.
PMSM	Permanent magnet synchronous machine.
PWM	Pulse width modulation.
VSI	Voltage source inverter.
SPWM	Sinusoidal PWM.
SVPWM	Space vector PWM.
ZSVIPWM	zero-sequence voltage injection PWM.
$u_{in}, u_{bus}, u^*_{bus}$	DC-source voltage, DC-bus voltage, DC-bus voltage reference.
u_{XN}, u^*_{XN}	Motor actual phase-voltage and phase-voltage reference, ($X \in A, B, C$).
u^*_{XN1}	Fundamental component of u^*_{XN}.
u_{XNamp}	Amplitude of u^*_{XN}.
u_{XN1amp}	Amplitude of u^*_{XN1}.
u_d, u_q, u_0	Motor phase-voltages in d-q-0 coordinate.
u_{ZS}	Motor zero-sequence voltage.
u_{AO}, u_{BO}, u_{CO}	Inverter pole-voltages in A-B-C coordinate.
u_{dO}, u_{qO}, u_{0O}	Inverter pole-voltages in d-q-0 coordinate.
i_A, i_B, i_C	Motor phase-currents in A-B-C coordinate.
i_d, i_q, i_0	Motor phase-currents in d-q-0 coordinate.
i_N, i_{bus}	Neutral current, DC-bus current.
L_d, L_q, L_0	d-axis, q-axis, zero-sequence inductance.
R	Phase-resistance.
ω_e, ω, θ_e	Rotor electrical speed, rotor mechanical speed, electrical position.
T_e	Electromagnetic torque.
ψ_f	Permanent magnet flux linkage.
α_X	Duty-cycle of inverter's upper switch, ($X \in A, B, C$).
α_d, α_q, α_0	The values of α_A, α_B, α_C converted to d-q-0 coordinate.
α_h	Inverter's mean duty-cycle.
C	DC-bus capacitance.
ω_n, T_n, P_n	Motor rated speed, rated torque, rated power.
p	Motor pole pairs.
f, T_s	Switching frequency, PWM period.

Manuscript received April 30, 2020; revised July 06, 2020; accepted July 23, 2020. (*Corresponding author: Xiaokang Zhang*).

The authors are with the laboratory Ampère (CNRS UMR5005), University of Lyon, Institut National des Sciences Appliquées de Lyon, 69621 Villeurbanne, France (e-mail: xiaokang.zhang@insa-lyon.fr; jean-yves.gauthier@insa-lyon.fr; xuefang.shi@insa-lyon.fr; romain.delpoux@insa-lyon.fr; jean-francois.tregouet@insa-lyon.fr).

I. INTRODUCTION

DUE to the advantages of high power density, high efficiency and wide speed regulation range, three-phase PMSM drives have been investigated for many years and extensively applied to a variety of industrial applications, such as machine tools, robotics, EVs, HEVs and aerospace [1]–[4]. The three-phase two-level VSI is the standard topology (see Fig. 1(a)) to drive a three-phase PMSM thanks to its compact structure. Generally speaking, the DC-source is supplied from the front end of inverter, and the motor's neutral point is unused [5]. Regarding the DC-source with limited voltage, such as the battery pack of EVs and HEVs whose voltage class is insufficient to meet the drive requirement, extra DC/DC converters are typically employed to boost the battery pack voltage and to exchange the energy between the battery

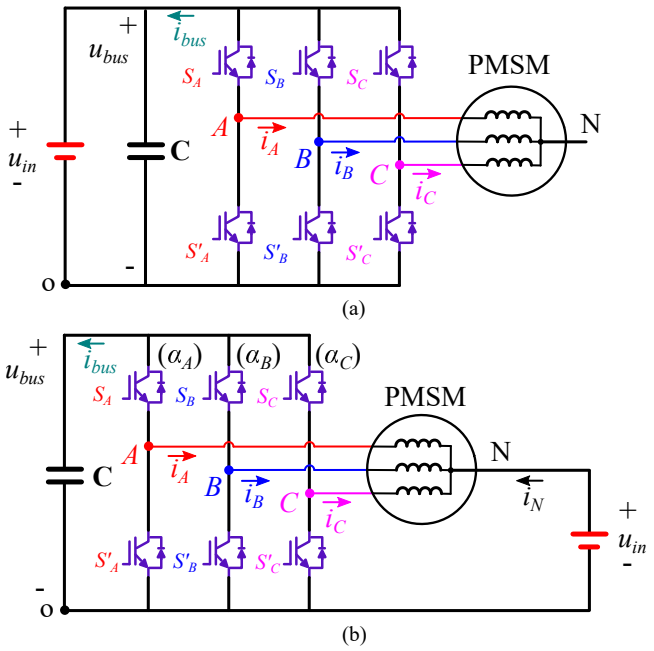

Fig. 1. PMSM drive topologies. (a) The standard topology. (b) The MFCS.

pack and DC-bus [6]. Apparently, the use of extra DC/DC converters sacrifices the volume, weight and cost of the whole system.

The MFCS presented in [7]–[10] gives a promising solution for the aforementioned issue because it has a free DC-voltage regulation function. As shown in Fig. 1(b), the MFCS evolves from the standard topology with the same components. But its DC-source is connected to the neutral point of the motor. With a zero-sequence voltage compensation strategy [10], the MFCS can drive the motor and regulate the DC-bus voltage simultaneously without physical DC/DC converters. The essence of the MFCS is utilizing the zero-sequence inductance of the motor and the inverter to indirectly construct an equivalent DC/DC converter function. Therefore, the MFCS can provide a compact and cost-saving solution for certain motor drives, especially the electric propulsion system of EVs and HEVs.

However, the zero-sequence voltage compensation strategy proposed in [10] is an open-loop control manner for the DC-bus voltage. The compensated voltage is derived from a steady-state equation in which the differential term of zero-sequence current is neglected. Therefore, in some transient states such as acceleration, deceleration and sudden load-change conditions, this strategy is insufficient to maintain a constant DC-bus voltage. In other words, the non-constant and fluctuant DC-bus voltage will deteriorate the motor performance, produce larger torque ripple and increase the overvoltage risk on the semi-conductor devices. Although the authors in [10] further proposed a two-motor type MFCS by connecting the DC-source between the neutral points of two motors for suppressing current ripple and improving the DC-voltage regulation ratio, it also suffers from the open-loop control strategy for the DC-bus voltage. In addition, only steady-state experiments were presented in [7]–[10]. In order to improve the dynamic performance of the MFCS, a closed-loop control for the DC-bus voltage is necessary. However, it is not easy to find a control DOF for the DC-bus voltage because the switching states of the inverter are determined by the control of the motor. Recently, [11] and [12] respectively studied the similar idea as the MFCS on a three-phase induction machine and a three-phase PMSM. Unfortunately, neither of them proposed a closed-loop control strategy for the DC-bus voltage. By connecting the battery pack to the neutral point of a traction motor, [13] proposed a low-cost electric propulsion system for HEVs. Compared with the MFCS, this scheme employs an auxiliary chopper so that a control DOF for the neutral current is provided. Some remarkable experimental results with dynamic tests were presented in [13]. Similarly, the improved MFCS with galvanic isolation for EVs was proposed in [14]–[16] by adding auxiliary choppers. However, it is not an ideal solution to improve the dynamic performance of the MFCS by using auxiliary choppers because it will increase the volume, weight and cost of the whole system, which seems to go against the original intention of the MFCS.

There is not much literature focusing on the topic of the MFCS and few deeper study is achieved. Besides, the comparative studies with the standard topology are also missing to distinguish the merits and drawbacks of the MFCS. Therefore, this paper intends to comprehensively explore the mechanism of the MFCS and its overall control strategy. The paper is organized as follows: In Section II, a brief description of the MFCS and its control challenge are introduced. An average model of the MFCS is built. Furthermore, an equivalent circuit is developed which clearly explains the intrinsically integrated DC-voltage regulation function. The inverter's mean duty-cycle is identified as an independent control DOF for the DC-bus voltage. In Section III, the influence on the DC-bus voltage caused by PWM behaviors is discussed. The ZSVIPWM is proposed to replace SVPWM and SPWM. Based on the ZSVIPWM, an overall control strategy is proposed in Section IV. In Section V, comparative experiments are performed. Finally, the main results are summarized in the Conclusion.

II. Analytical Modeling

The MFCS consists of a DC-bus capacitor, a three-phase two-level VSI, a three-phase PMSM and a DC-source which is connected to the neutral point 'N', as shown in Fig. 1(b). S_A, S_B, S_C and $S_A^{'}$, $S_B^{'}$, $S_C^{'}$ are the complementary PWM signals. Looking from left to right, the MFCS is a motor drive in which the neutral point 'N' is clamped to u_{in}. Looking from right to left, the MFCS is like a three-phase DC/DC converter but the motor's back-EMFs are the disturbances of u_{in}. Normally, for three-phase AC motor drives, the switching states of the inverter are determined by SVPWM or SPWM according to motor control algorithms. For three-phase DC/DC converters, the interleaved PWM with 120° phase-shifted are typically used [17]. As for the MFCS, the key point is to find the independent control DOFs respectively for controlling the motor and the DC-bus voltage only by one inverter.

A. Average Model

The average modeling method is adopted in this paper. Defining the average value of a variable $x(t)$ in one PWM period (T_s) as

$$\overline{x}(t) = \frac{1}{T_s}\int_{t-T_s}^{t} x(\tau)d\tau \tag{1}$$

When considering an ideal inverter, voltage drop and dead time are neglected. The average voltage equation of the MFCS can be formulated by

$$\begin{bmatrix}\overline{u}_{AO}\\ \overline{u}_{BO}\\ \overline{u}_{CO}\end{bmatrix} = \begin{bmatrix}\alpha_A\\ \alpha_B\\ \alpha_C\end{bmatrix}\overline{u}_{bus} = \begin{bmatrix}\overline{u}_{AN}\\ \overline{u}_{BN}\\ \overline{u}_{CN}\end{bmatrix} + \begin{bmatrix}\overline{u}_{in}\\ \overline{u}_{in}\\ \overline{u}_{in}\end{bmatrix} \tag{2}$$

The average current equations of the MFCS can be formulated by

$$\begin{aligned}\bar{i}_{bus} = C\frac{d\overline{u}_{bus}}{dt} &= -\begin{bmatrix}\alpha_A\\ \alpha_B\\ \alpha_C\end{bmatrix}^T\begin{bmatrix}\bar{i}_A\\ \bar{i}_B\\ \bar{i}_C\end{bmatrix}\\ &= -\boldsymbol{\alpha}_{ABC}^T\bar{\boldsymbol{i}}_{ABC}\end{aligned} \tag{3}$$

$$\bar{i}_A + \bar{i}_B + \bar{i}_C + \bar{i}_N = 0 \tag{4}$$

where $\boldsymbol{\alpha}_{ABC}^T$ is the duty-cycle vector; $\bar{\boldsymbol{i}}_{ABC}$ represents the phase-current vector.

By using the Park transformation ($\boldsymbol{T}_p$)

$$\boldsymbol{T}_p = \sqrt{\frac{2}{3}}\begin{bmatrix}\cos\theta_e & \cos\left(\theta_e-\frac{2\pi}{3}\right) & \cos\left(\theta_e+\frac{2\pi}{3}\right)\\ -\sin\theta_e & -\sin\left(\theta_e-\frac{2\pi}{3}\right) & -\sin\left(\theta_e+\frac{2\pi}{3}\right)\\ \sqrt{\frac{1}{2}} & \sqrt{\frac{1}{2}} & \sqrt{\frac{1}{2}}\end{bmatrix} \tag{5}$$

(2) can be transformed from A-B-C to d-q-0 coordinates, as

$$\begin{bmatrix}\overline{u}_{dO}\\ \overline{u}_{qO}\\ \overline{u}_{0O}\end{bmatrix} = \begin{bmatrix}\alpha_d\\ \alpha_q\\ \alpha_0\end{bmatrix}\overline{u}_{bus} = \begin{bmatrix}\overline{u}_d\\ \overline{u}_q\\ \overline{u}_0\end{bmatrix} + \begin{bmatrix}0\\ 0\\ \sqrt{3}\,\overline{u}_{in}\end{bmatrix} \tag{6}$$

In addition, the mathematical model of the PMSM in d-q-0 coordinate can be formulated by

$$\begin{aligned}\begin{bmatrix}\overline{u}_d\\ \overline{u}_q\\ \overline{u}_0\end{bmatrix} &= \begin{bmatrix}R & 0 & 0\\ 0 & R & 0\\ 0 & 0 & R\end{bmatrix}\begin{bmatrix}\bar{i}_d\\ \bar{i}_q\\ \bar{i}_0\end{bmatrix} + \begin{bmatrix}L_d & 0 & 0\\ 0 & L_q & 0\\ 0 & 0 & L_0\end{bmatrix}\frac{d}{dt}\begin{bmatrix}\bar{i}_d\\ \bar{i}_q\\ \bar{i}_0\end{bmatrix}\\ &\quad + \overline{\omega}_e\begin{bmatrix}-L_q\bar{i}_q\\ L_d\bar{i}_d+\psi_f\\ 0\end{bmatrix}\end{aligned} \tag{7}$$

Substituting (7) into (6), the 0-axis term of (6) becomes

$$\alpha_0\overline{u}_{bus} = \overline{u}_0 + \sqrt{3}\overline{u}_{in} = R\bar{i}_0 + L_0\frac{d\bar{i}_0}{dt} + \sqrt{3}\overline{u}_{in} \tag{8}$$

According to the Park transformation ($\boldsymbol{T}_p$), $\bar{i}_0 = (\bar{i}_A+\bar{i}_B+\bar{i}_C)/\sqrt{3}$. Combining this with (4), it gives $\bar{i}_0 = -\bar{i}_N/\sqrt{3}$. Therefore, (8) can be reformulated as

$$\overline{u}_{in} = \frac{R}{3}\bar{i}_N + \frac{L_0}{3}\frac{d\bar{i}_N}{dt} + \frac{\alpha_0}{\sqrt{3}}\overline{u}_{bus} \tag{9}$$

Because α_A, α_B and α_C are strictly limited between 0 and 1, the value of $\alpha_0/\sqrt{3} = (\alpha_A+\alpha_B+\alpha_C)/3$ is also restricted between 0 and 1. For convenience, the inverter's mean duty-cycle (α_h) is defined as

$$\alpha_h = \frac{(\alpha_A+\alpha_B+\alpha_C)}{3} = \frac{\alpha_0}{\sqrt{3}} \tag{10}$$

Substituting (10) into (9), (9) becomes

$$\overline{u}_{in} = \frac{R}{3}\bar{i}_N + \frac{L_0}{3}\frac{d\bar{i}_N}{dt} + \alpha_h\overline{u}_{bus} \tag{11}$$

Equation (11) is similar to the average model of a single-phase DC/DC converter, with $R/3$ as the parasitic resistance, $L_0/3$ as the filtering inductance and α_h as the duty-cycle of the chopper. Therefore, from the average model point of view, the MFCS integrates the possibility of regulating the DC-bus voltage. By omitting $R/3$, $\overline{u}_{bus}\approx\overline{u}_{in}/\alpha_h$ in steady-state. In order to clearly detail the correlations between the DC-bus voltage and the motor, an equivalent circuit of the MFCS will be developed in the following.

B. Equivalent Circuit

Conducting the following transformations to (3), $\bar{i}_{bus}$ becomes

$$\begin{aligned}\bar{i}_{bus} &= -\boldsymbol{\alpha}_{ABC}^T(\boldsymbol{T}_p^{-1}\boldsymbol{T}_p)\bar{\boldsymbol{i}}_{ABC} = -(\boldsymbol{\alpha}_{ABC}^T\boldsymbol{T}_p^{-1})(\boldsymbol{T}_p\bar{\boldsymbol{i}}_{ABC})\\ &= -((\boldsymbol{T}_p^{-1})^T\boldsymbol{\alpha}_{ABC})^T(\boldsymbol{T}_p\bar{\boldsymbol{i}}_{ABC})\\ &= -(\boldsymbol{T}_p\boldsymbol{\alpha}_{ABC})^T(\boldsymbol{T}_p\bar{\boldsymbol{i}}_{ABC})\\ &= -\begin{bmatrix}\alpha_d\\ \alpha_q\\ \alpha_0\end{bmatrix}^T\begin{bmatrix}\bar{i}_d\\ \bar{i}_q\\ \bar{i}_0\end{bmatrix} = -\alpha_d\bar{i}_d - \alpha_q\bar{i}_q - \alpha_0\bar{i}_0\\ &= -\alpha_d\bar{i}_d - \alpha_q\bar{i}_q + \alpha_h\bar{i}_N\end{aligned} \tag{12}$$

It is known that FOC makes it feasible to control an AC motor as a separately excited DC motor by decoupling the torque and flux linkage. Therefore, the PMSM is equivalent to a DC motor in d-q coordinate. By defining a virtual chopper as 'C1' and two virtual H-bridges respectively as 'H1' and 'H2', the MFCS can be converted to a cascaded DC/DC converter-DC motor drive system, as shown in Fig. 2. The PWM signals of the virtual switches $S_{vn}(n = 1,2,3,4,5)$ are complementary with those of $S_{vn}^{'}$. α_h represents the duty-cycle of S_{v1}, α_d represents the difference between the duty-cycles of S_{v3} and S_{v4}, and α_q represents the difference between the duty-cycles of S_{v2} and S_{v5}. The explanations of the equivalent circuit are as follows:

According to Kirchhoff's Voltage Law, (11) is visualized by the contour 'K' in Fig. 2. In the same way, the relationships of $\overline{u}_d = \alpha_d\overline{u}_{bus}$ and $\overline{u}_q = \alpha_q\overline{u}_{bus}$ in (6) are visualized by the double H-bridges circuit 'H1' and 'H2'. The current relation in (12) is visualized on the node 'P' according to Kirchhoff's Current Law. e_d and e_q are respectively equal to $-\overline{\omega}_e L_q\bar{i}_q$ and $\overline{\omega}_e(L_d\bar{i}_d+\psi_f)$ according to (7).

Consequently, the equivalent circuit explicitly reveals an EDC function exists in the MFCS. The PMSM can be seen as an equivalent load of the EDC. Meanwhile, it also reveals that the motor and the EDC are uncoupled in d-q-0 coordinate. Hence, α_h can be an independent control DOF of the EDC.

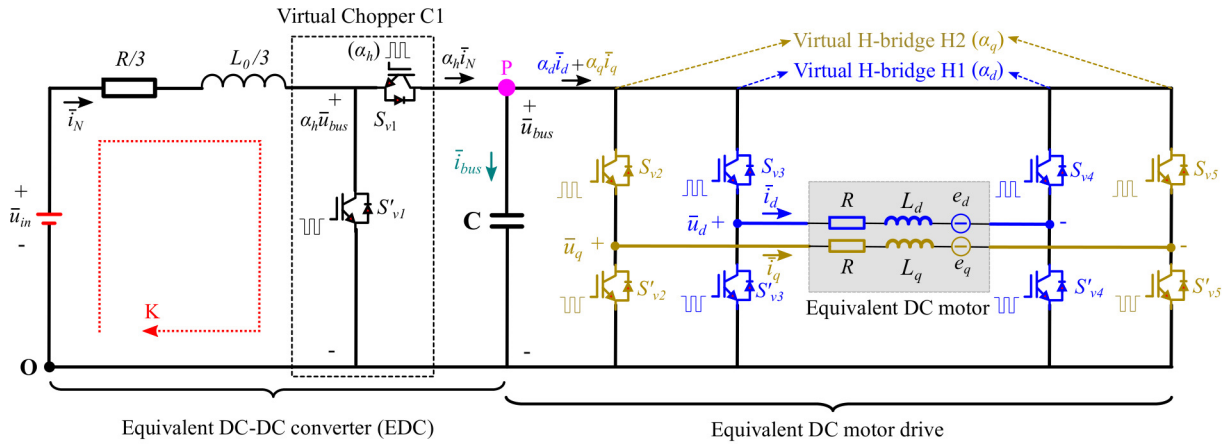

Fig. 2. Equivalent circuit of the MFCS.

III. ZSVIPWM

Thanks to its high output quality, SVPWM is chosen preferentially in many PMSM drives [18]. The modulation ratio m (fundamental voltage amplitude to carrier amplitude) of SVPWM can reach 1.15 in the absence of overmodulation [19] [20]. For the MFCS, the inverter's mean duty-cycle α_h should be analyzed before using PWM technologies since the existence of the EDC. According to the SVPWM algorithm, the evolution of α_h with m in one fundamental period is shown in Fig. 3 [21]. It can be seen that for a given m, α_h is almost a triangular wave. Its mean value is 0.5 and its frequency is three times the frequency the fundamental wave. The amplitude of α_h increases with the increasing of m. When $m = 1.15$, the peak and valley points of α_h reach around 0.66 and 0.34 respectively. According to the EDC phenomenon, the DC-bus voltage will be fluctuant with the same frequency of α_h if SVPWM is employed in the MFCS. Especially, the oscillation amplitude will be $(1/0.34 - 1/0.66)\overline{u}_{in} \approx 1.43\,\overline{u}_{in}$ when $m = 1.15$. Such large oscillations will deteriorate the motor performance undoubtedly. Thus, SVPWM is inapplicable for the MFCS. To address this problem, the ZSVIPWM will be proposed in the following.

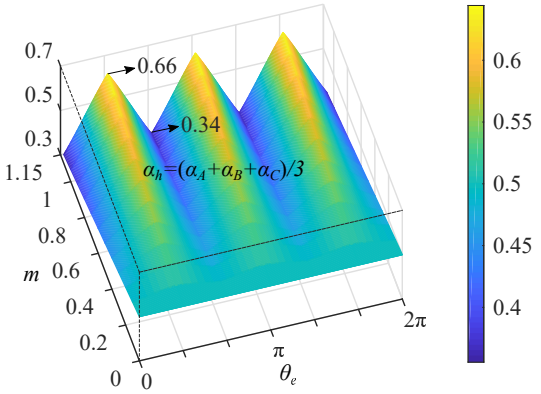

Fig. 3. The inverter's mean duty-cycle α_h under SVPWM.

A. Zero-sequence Voltage and Duty-cycle Calculations

For the MFCS, a certain amount of zero-sequence voltage is necessary. The requisite zero-sequence voltage ($\overline{u}_{ZS}$) can be expressed by

$$\overline{u}_{ZS} = \frac{(\overline{u}_{AN} + \overline{u}_{BN} + \overline{u}_{CN})}{3} = \frac{\overline{u}_0}{\sqrt{3}} \tag{13}$$

According to (8) and (10)

$$\overline{u}_{ZS} = \frac{\overline{u}_0}{\sqrt{3}} = \alpha_h \overline{u}_{bus} - \overline{u}_{in} \tag{14}$$

Therefore, the actual phase-voltage reference $\overline{u}_{XN}{}^*$ can be expressed as

$$\overline{u}_{XN}{}^* = \overline{u}_{XN1}{}^* + \overline{u}_{ZS} = \overline{u}_{XN1}{}^* + \alpha_h \overline{u}_{bus} - \overline{u}_{in} \tag{15}$$

Because of the clamped neutral point, the positive and negative amplitudes of carrier signals in the MFCS are respectively $\overline{u}_{bus} - \overline{u}_{in}$ and $-\overline{u}_{in}$, as shown in Fig. 4(a). According to the regular-sampling method (see Fig. 4(b)), the duty-cycle α_X is derived as

$$\alpha_X = \frac{\delta/2}{T_s/2} = \frac{\overline{u}_{XN}{}^* + \overline{u}_{in}}{\overline{u}_{bus}} = \alpha_h + \frac{\overline{u}_{XN1}{}^*}{\overline{u}_{bus}} \tag{16}$$

in which δ is the high-level time of S_X in one PWM period.

Consequently, (16) is the final algorithm of the ZSVIPWM. Especially, when $\alpha_h = 0.5$, (16) corresponds to the algorithm of SPWM. However, SPWM can merely regulate $\overline{u}_{bus}$ to 2 times of $\overline{u}_{in}$ in an open-loop way. The proposed ZSVIPWM can flexibly adjust $\overline{u}_{bus}$ to different values in a closed-loop way thanks to the EDC.

B. DC-source Utilization Ratio (DCSUR)

Due to the EDC, the DC-bus voltage $\overline{u}_{bus}$ can reach higher value than $\overline{u}_{in}$. But the reachable AC-voltages for the motor are bounded. The step-up ratio (r_0) of the EDC and the DCSUR (r_1) are respectively defined as

$$\begin{aligned} r_0 &= \frac{\overline{u}_{bus}}{\overline{u}_{in}} \\ r_1 &= \frac{u_{XN1amp}}{\overline{u}_{in}} \end{aligned} \tag{17}$$

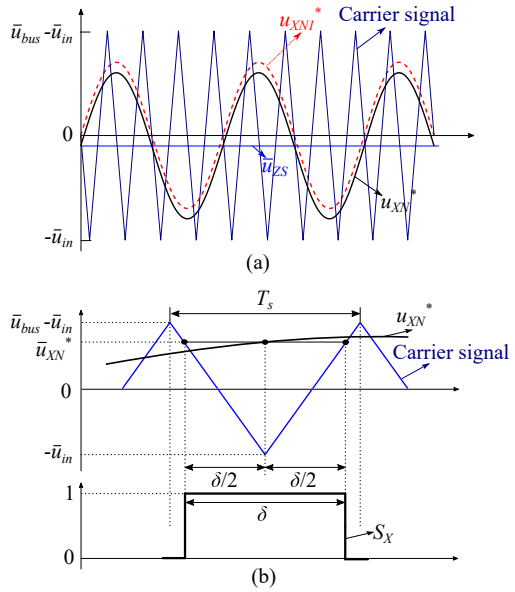

Fig. 4. The schematic diagram of the proposed ZSVIPWM. (a) Carrier comparison. (b) Regular-sampling method.

The zero-sequence voltage ratio (r_2) is defined as

$$r_2 = \frac{|\overline{u}_{ZS}|}{\overline{u}_{in}} \tag{18}$$

In order to guarantee $u_{XN}{}^*$ within the linear modulation region, u_{XNamp} is limited by the smaller one between $\overline{u}_{in}$ and $\overline{u}_{bus} - \overline{u}_{in}$. Thus, u_{XN1amp} is also limited. As shown in Fig. 5(a), when $\overline{u}_{bus} > 2\overline{u}_{in}$ (i.e. $r_0 > 2$), the carrier signal is asymmetrical because $\overline{u}_{bus} - \overline{u}_{in}$ is larger than $\overline{u}_{in}$. Meanwhile, $u_{XN}{}^*$ shows a downward offset because of the injected zero-sequence voltage $\overline{u}_{ZS}$. It is obvious that the limit of u_{XNamp} is $\overline{u}_{in}$. Therefore, the limit of u_{XN1amp} is $\overline{u}_{in} - |\overline{u}_{ZS}|$ (i.e. $r_1 = 1 - r_2$). Similarly, r_1 can be analyzed in the same way when $\overline{u}_{in} < \overline{u}_{bus} \le 2\overline{u}_{in}$ (i.e. $1 < r_0 \le 2$). The analysis results are summarized as follows: when $r_0 > 2$, $r_1 = 1 - r_2$; when $1 < r_0 \le 2$, $r_1 = r_0 + r_2 - 1$. For the sake of explanations, the curves of r_1 are visualized in Fig. 5(b). For a certain r_2, r_1 maintains $1 - r_2$ when $r_0 \ge (2 - 2r_2)$. r_1 decreases with the decrease of r_0 when $1 < r_0 < (2 - 2r_2)$. Therefore, the largest DCSUR is $1 - r_2$ and the point 'a' ($r_0 = 2 - 2r_2$) is the optimal operating point for the whole system. When r_2 reduces to r_2', r_1 becomes r_1'. In this case, the largest DCSUR increases to $1 - r_2'$ and the best operating point moves to 'b'. Further, when r_2 reduces to 0, r_1 becomes r_1''. In this case, the largest DCSUR is 1 and the best operating point moves to the point '2' ($\overline{u}_{bus} = 2\overline{u}_{in}$).

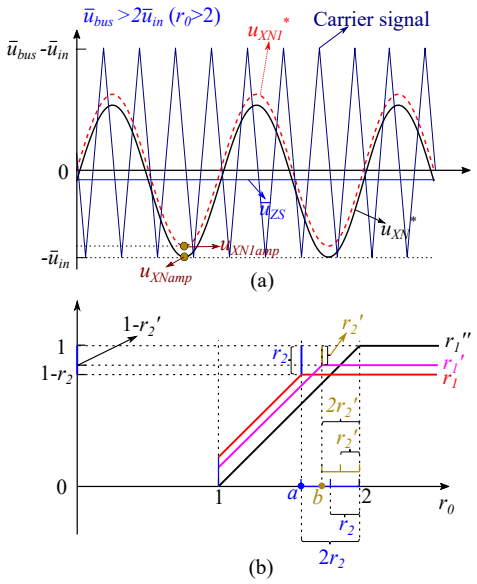

Fig. 5. The DCSUR analyses of the MFCS. (a) When ($r_0 > 2$). (b) Analysis results.

In steady-state, the differential term of (11) $\frac{L_0}{3}\frac{d\bar{i}_N}{dt} = 0$. Combining with (14), $\overline{u}_{ZS}$ is equal to $\frac{-R\bar{i}_N}{3}$. This means $|\overline{u}_{ZS}|$ is equal to the voltage drop in $R/3$. Generally speaking, the stator resistance of a PMSM is much less than its inductive reactance [15]. Therefore, r_2 is small. If r_2 is omitted, the largest DCSUR of the MFCS approximates to 1 and the maximum effective step-up ratio r_0 of the EDC is 2. According to the definition of DCSUR, the DCSUR of the standard topology is only 0.58 by using SVPWM [19].

IV. Control of The MFCS

According to the proposed ZSVIPWM algorithm in (16), the fundamental voltage $u_{XN1}{}^*$ and α_h are respectively the independent control DOFs for the motor and the EDC. Thus, it is feasible to control the motor and the EDC simultaneously by employing a FOC controller and a common DC/DC converter controller.

A. Overall Control Strategy

The overall control strategy of the MFCS is divided into three parts, as shown in Fig. 6. Firstly, the FOC controller includes two current-loops and one speed-loop. The PI controller of speed-loop outputs the q-axis current reference $i_q{}^*$. For a surface-mounted PMSM without flux-weakening demand, the d-axis current reference $i_d{}^* = 0$. The voltage references $u_d{}^*$ and $u_q{}^*$ are obtained by the two PI controllers of current-loops with decoupling compensation. By inverse

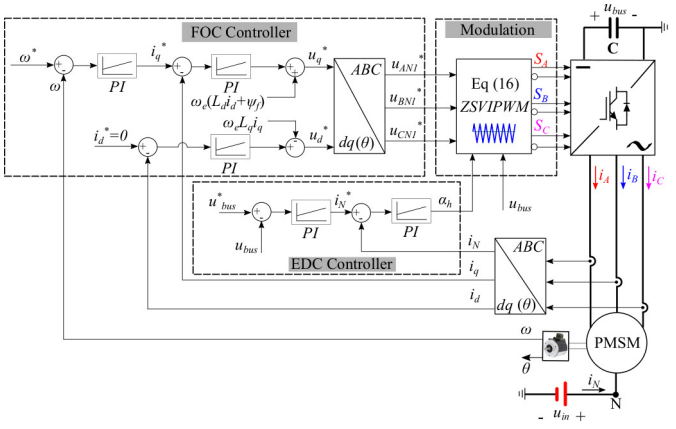

Fig. 6. The overall control strategy of the MFCS.

Park transformation, the fundamental voltage references are obtained. Secondly, a cascaded PI controller is used for the EDC. The PI controller of voltage-loop outputs the neutral current reference $i_N{}^*$ and the PI controller of current-loop outputs the inverter's mean duty-cycle α_h. After obtaining $u_{XN1}{}^*$ ($X \in A, B, C$) and α_h, the duty-cycles α_A, α_B and α_C are calculated according to proposed ZSVIPWM algorithm in (16). Finally, the PWM signals S_A, S_B, S_C and $S_A^{'}$, $S_B^{'}$, $S_C^{'}$ are generated by comparing these duty-cycles with a triangular signal in the microprocessor.

B. Small-Signal Model of the EDC

According to Fig. 2, the PMSM can be seen as an equivalent load (R_{Load}) of the EDC. Therefore, Fig. 2 can be simplified to Fig. 7. D represents the duty-cycle of $S_{v1}^{'}$ and $\alpha_h = 1 - D$ by neglecting the dead time. Without considering the losses, R_{Load} can be calculated approximatively as

$$R_{Load} \approx \frac{u_{bus}^{*2}}{P_n} \tag{19}$$

The equilibrium states (D_s and i_{Ns}) of the EDC are

$$\begin{cases} D_s = 1 - \dfrac{u_{in}}{u_{bus}^*} \\ i_{Ns} = \dfrac{u_{bus}^{*2}}{u_{in} R_{Load}} \end{cases} \tag{20}$$

Therefore, the small-signal model of the EDC can be built as

$$\begin{bmatrix} \dot{\tilde{i}}_N \\ \dot{\tilde{u}}_{bus} \end{bmatrix} = \begin{bmatrix} 0 & \dfrac{D_s - 1}{L_0/3} \\ \dfrac{1 - D_s}{C} & \dfrac{-1}{R_{Load} C} \end{bmatrix} \begin{bmatrix} \tilde{i}_N \\ \tilde{u}_{bus} \end{bmatrix} + \begin{bmatrix} \dfrac{u_{bus}^*}{L_0/3} \\ \dfrac{-i_{Ns}}{C} \end{bmatrix} \tilde{D} \tag{21}$$

According to the small-signal model, the system transfer functions can be derived as

$$H1(s) = \frac{\tilde{i}_N(s)}{\tilde{D}(s)} = \frac{\dfrac{u_{bus}^*}{L_0/3} s + \dfrac{u_{bus}^*}{R_{Load}(L_0/3)C} + \dfrac{(1 - D_s)}{(L_0/3)C} i_{Ns}}{s^2 + \dfrac{1}{R_{Load} C} s + \dfrac{(1 - D_s)^2}{(L_0/3)C}} \tag{22}$$

$$H2(s) = \frac{\tilde{u}_{bus}(s)}{\tilde{D}(s)} = \frac{\dfrac{-i_{Ns}}{C} s + \dfrac{(1 - D_s)}{(L_0/3)C} u_{bus}^*}{s^2 + \dfrac{1}{R_{Load} C} s + \dfrac{(1 - D_s)^2}{(L_0/3)C}} \tag{23}$$

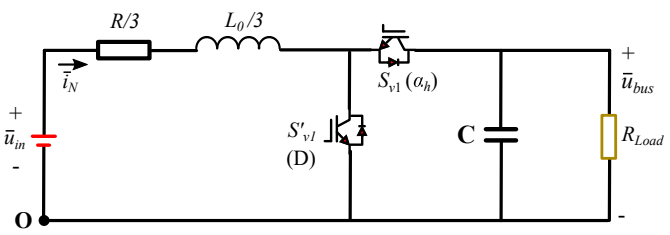

Fig. 7. The simplified equivalent circuit of the MFCS.

$$H3(s) = \frac{\tilde{u}_{bus}(s)}{\tilde{i}_N(s)} = \frac{H2(s)}{H1(s)} \tag{24}$$

According to $H1(s)$ and $H3(s)$, the PI parameters for the current-loop and voltage-loop of the EDC can be tuned.

V. Experimental Results

Experiments are carried out on a surface-mounted PMSM (whose neutral point is available) to verify the theoretical analyses, ZSVIPWM and overall control strategy, as well as to assess the MFCS. The parameters of the PMSM drive are: $u_{bus} = 30$ V, $C = 510$ uF, $P_n = 52.5$ W, $T_n = 125$ mN·m, $\omega_n = 4000$ rpm, $R = 0.6\ \Omega$, $L_d = L_q = 1.1$ mH, $L_0/3 = 0.26$ mH, $p = 4$, $\psi_f = 0.0056$ Wb, $f = 20$ kHz.

According to the analyses in Section III, the maximum effective step-up ratio of the EDC approximates to 2. Therefore, u_{in} is chosen as 15 V (half of u_{bus}). For contrast, the similar experiments are implemented on the PMSM fed by the standard topology, in which a 30 V u_{in} is required. The parameters of the FOC controllers in both topologies are identical. The algorithms are implemented on a dSPACE DS1202 MicroLabBox platform and the experiment setup is illustrated in Fig. 8. The torquemeter and hysteresis brake used in this test-bench are MAGTROL TM-303 and HB-450 respectively.

For the MFCS, the DC-bus voltage needs to be raised to 30 V before starting the motor. As shown in Fig. 9, u_{bus} is 15 V before the startup. When the EDC runs, u_{bus} is boosted to 30 V with 5 V overshoots and it tends to stable state rapidly. This demonstrates the EDC phenomenon of the MFCS.

A. Steady-state Performance

Fig. 10 illustrates the steady-state performance respectively conducted by the MFCS and standard topology when the motor operates at rated condition (4000 rpm and 125 mN·m).

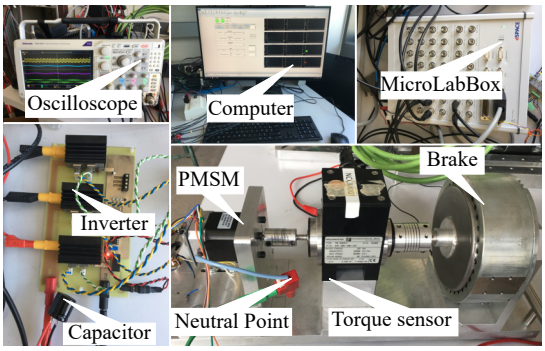

Fig. 8. Experiment setup.

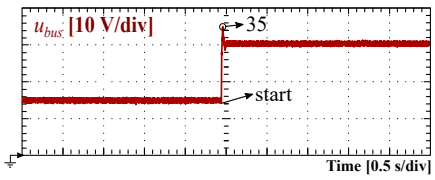

Fig. 9. The DC-bus voltage of the MFCS during a startup process.

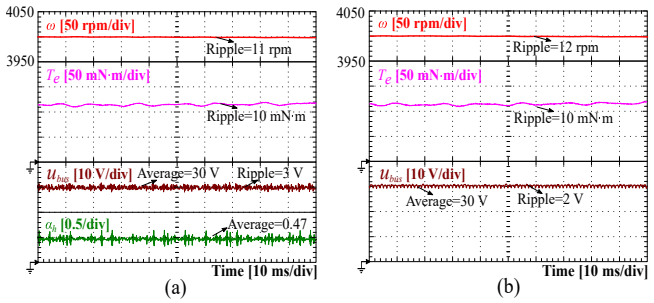

Fig. 10. Steady-state performance (speed, torque and DC-bus voltage) at rated condition. (a) The MFCS with 15 V DC-source. (b) The standard topology with 30 V DC-source

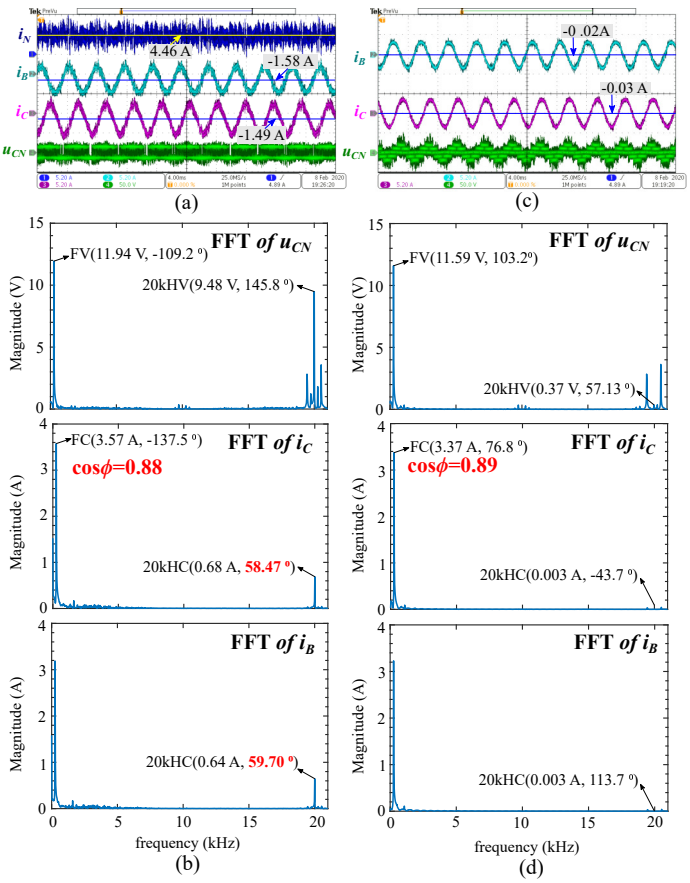

Fig. 11. Steady-state performance (neutral current, phase-currents, phase-voltages and FFT analyses) at rated condition. (a), (b) The MFCS with 15 V DC-source. (c), (d) The standard topology with 30 V DC-source.

For the results of the MFCS, it can be seen that u_{bus} is boosted at 30 V stably while α_h is around 0.47 (considering the voltage drop in $R/3$, α_h is not exactly 0.5). This verifies the correctness of the theoretical analyses presented in this paper. The rotor speed ω remains stable at 4000 rpm with slight fluctuations of 11 rpm (0.27%). The electromagnetic torque T_e maintains 125 mN·m stably with 10 mN·m (8%) fluctuations. For the standard topology, a stable 30 V DC-source is connected to the DC-bus directly. The ripple of u_{bus} is only caused by the charge-discharge of the DC-bus capacitor in different switching states. However, for the MFCS, u_{bus} has to be controlled at 30 V by the EDC function. The ripple of u_{bus} results from not only the charge-discharge of the DC-bus capacitor but also the control errors of the EDC. Therefore, it can be seen that the voltage ripple of the MFCS is a little larger than that of the standard topology (3 V to 2 V). Even so, the motor performance (speed and torque ripple) of both topologies is similar.

In order to evaluate the characteristics of voltages and currents, the real-time datum recorded by the Tektronix oscilloscope MDO3000 (which can record 1 M points in 40 ms period) are shown in Fig. 11(a) and (c). Firstly, in Fig. 11(a), it can be seen that the mean values of i_B and i_C are respectively -1.58 A and -1.49 A. This means the phase-currents of the MFCS shift downward because of the zero-sequence current. The offset value approximates to -1/3 the mean value of i_N (4.46 A). Comparatively speaking, the phase-currents of the standard topology are symmetrical whose mean values are near 0 A, as shown in Fig. 11(c). Secondly, Fig. 11(a) shows u_{CN} of the MFCS only has two voltage-levels, $u_{bus} - u_{in}$ (15 V) and $-u_{in}$ (-15 V) because of the clamped neutral point. u_{CN} of the standard topology has five voltage-levels $\pm\frac{1}{3}u_{bus}$ ($\pm$10 V), 0 V and $\pm\frac{2}{3}u_{bus}$ ($\pm$20 V) thanks to the floating neutral point, as shown in Fig. 11(c).

The FFT analyses of u_{CN}, i_B and i_C in both topologies are shown in Fig. 11 (b) and (d). Firstly, the fundamental voltage (FV) amplitude and fundamental current (FI) amplitude are respectively 11.94 V and 3.57 A in the MFCS while they are respectively 11.59 V and 3.37 A in the standard topology. The fundamental power factor $cos\phi$ is about 0.88 in the MFCS while it is 0.89 in the standard topology. Comparatively speaking, these fundamental characteristics of both topologies are similar. Secondly, for the MFCS, the zero-sequence current flowing into the motor coils undoubtedly produces more losses in the motor. In order to calculate the total active power of the motor, an easy method of accumulating the power generated by all the harmonics (including zero-sequence and fundamental components) is adopted. The result indicates that the total active power of the motor in the MFCS increases by 6.02 W compared to that in the standard topology. Therefore, it can be concluded that the increased motor losses in the MFCS is about 11.5% of P_n at rated condition. The increased copper losses caused by the zero-sequence current are just the power consumed in $R/3$, which can be calculated by $\bar{i}_N{}^2\frac{R}{3} = 3.98$ W (7.6% to P_n). Therefore, the increased iron losses are about 2.04 W (3.9% to P_n). Although the motor losses of the MFCS increase, they can be mitigated by proper design of motor winding layout with larger L_0. For example, [22] and [23] presented that a motor with a two-layer fractional slot winding has bigger leakage inductance than the motor with side-by-side placed winding. Thirdly, the 20 kHz harmonic voltage (20kHV) amplitude of u_{CN} in the MFCS is larger than that in the standard topology (9.48 V to 0.37 V). Thus, it can be seen that the 20 kHz harmonic current (20kHC) amplitude of i_C in the MFCS is also larger than that in the standard topology (0.68 A to 0.003 A). However, the 20kHC in the MFCS does not affect the electromagnetic torque because the 20kHCs of

i_B and i_C almost have the same amplitude (0.68 A to 0.64 A) and phase position (58.47° to 59.70°). In other words, the 20kHCs do not generate harmonic torque. Therefore, although the phase-current ripple of the MFCS is larger, the torque performance can be maintained.

B. Dynamic Performance

The dynamic tests including speed regulation and sudden loading/deloading are shown in Fig. 12. On the one hand, ω^* is set to 1000 rpm before 2 s, and it is 2000 rpm between 2 and 6 s, after which it is reset to 1000 rpm. On the other hand, the load torque is 40 mN·m before 10 s. Then it is set to 120 mN·m at 10 s and reduced to 40 mN·m again at 15 s.

In Fig. 12(a), it can be seen that u_{bus} of the MFCS can remain relatively stable at 30 V during the acceleration, deceleration, loading and deloading processes. Specifically, when the motor accelerates suddenly, it means the equivalent load of the EDC increases instantly. In order to withstand the voltage sag, the controller of the EDC decreases α_h sharply so that i_N increases quickly for providing more power for

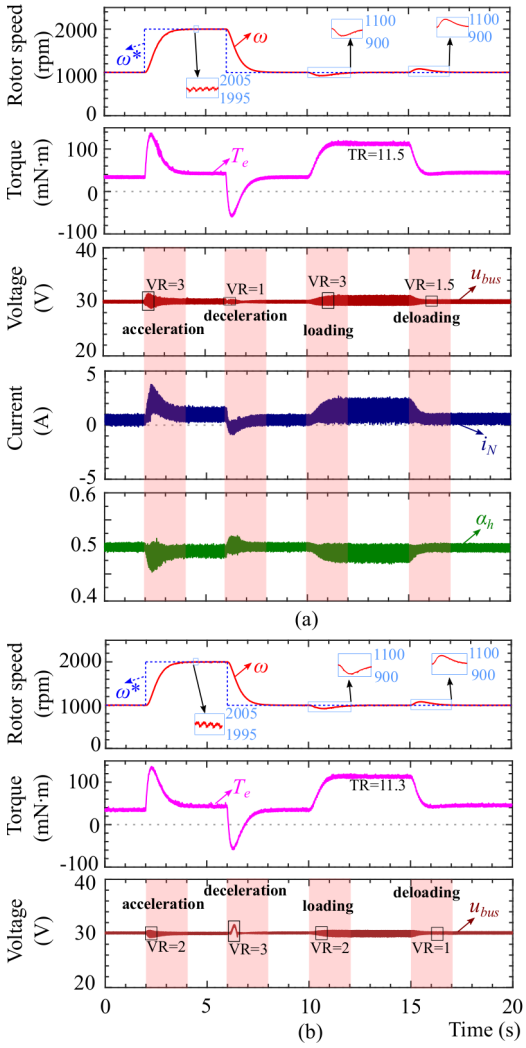

Fig. 12. Dynamic performance. (a) The MFCS with 15 V DC-source. (b) The standard topology with 30 V DC-source.

TABLE I
THE MAIN CHARACTERISTICS OF THE MFCS COMPARED TO THE STANDARD TOPOLOGY

Characteristic	Evaluation
Speed control performance	Similar
Torque ripple performance	Similar
DCSUR	Larger (1 vs 0.58)
Integrated EDC function	YES vs NO
Current ripple	Bigger
Losses	Bigger (11.5% for the test PMSM)

the system. Consequently, u_{bus} shows 3 V fluctuations at the beginning of the acceleration then it tends to be stable with 2 V voltage ripple (VR). For the standard topology in the same condition, u_{bus} also shows a 2 V VR when the motor accelerates instantly. During the deceleration process, the motor becomes a generator. In order to prevent the voltage rise, the controller of the EDC increases α_h sharply so that i_N decreases to negative values for bleeding the increasing power stored in the DC-bus capacitor. Therefore, u_{bus} scarcely appears overshoot in the MFCS. Without the EDC function, u_{bus} of the the standard topology shows a 3 V overshoot.

For both topologies, the rotor speed can track the reference well without overshoot in the acceleration and deceleration processes. When the load is applied and removed, the speed shows slight dip (40 rpm) but it turns to stable state quickly. The torque ripple (TR) is around 11 mN·m in both topologies. Comparatively speaking, the motor dynamic performance of the MFCS is same as that of the standard topology.

In general, the main characteristics of the MFCS compared to the standard topology are summarized in Table. I.

VI. CONCLUSION

In this paper, the comprehensive studies of the MFCS are presented. Thanks to a rigorous modeling, the inverter's mean duty-cycle is identified as an independent control DOF for the EDC. It makes possible to control the EDC in a closed-loop way without auxiliary choppers. The proposed overall control strategy is simple, in which the FOC can still be used without modifications to control the motor and a cascaded PI controller is sufficient to control the EDC. The convincing experiments verify the effectiveness of the proposed control strategy. Although the motor losses increase, the MFCS provides a promising solution for AC motor drives with lower cost and smaller volume when the DC-source is limited.

The main contributions of this paper are summarized as follows:

1) An equivalent circuit is developed to clearly reveals the mechanism of the MFCS.
2) The inverter's mean duty-cycle is identified as an independent control DOF for the EDC.
3) The ZSVIPWM is proposed for the MFCS to replace SPWM and SVPWM .
4) An overall control strategy is proposed for the MFCS, in which the motor and the EDC can be controlled independently.

REFERENCES

[1] J. Lara, J. Xu, and A. Chandra, "Effects of rotor position error in the performance of field-oriented-controlled PMSM drives for electric vehicle traction applications," *IEEE Trans. Ind. Electron.*, vol. 63, no. 8, pp. 4738–4751, 2016.

[2] J. Lu, X. Zhang, Y. Hu, J. Liu, C. Gan, and Z. Wang, "Independent phase current reconstruction strategy for IPMSM sensorless control without using null switching states," *IEEE Trans. Ind. Electron.*, vol. 65, no. 6, pp. 4492–4502, 2018.

[3] S. Xiao, X. Gu, Z. Wang, T. Shi, and C. Xia, "A novel variable DC-link voltage control method for PMSM driven by a quasi-z-source inverter," *IEEE Trans. Power Electron.*, vol. 35, no. 4, pp. 3878–3890, 2020.

[4] J. Yang, W. Chen, S. Li, L. Guo, and Y. Yan, "Disturbance/uncertainty estimation and attenuation techniques in PMSM drives-a survey," *IEEE Trans. Ind. Electron.*, vol. 64, no. 4, pp. 3273–3285, 2017.

[5] H. Yan, Y. Xu, F. Cai, H. Zhang, W. Zhao, and C. Gerada, "PWM-VSI fault diagnosis for a PMSM drive based on the fuzzy logic approach," *IEEE Trans. Power Electron.*, vol. 34, no. 1, pp. 759–768, 2019.

[6] H. Cheng, L. Wang, L. Xu, X. Ge, and S. Yang, "An integrated electrified powertrain topology with SRG and SRM for plug-in hybrid electrical vehicle," *IEEE Trans. Ind. Electron.*, vol. 67, no. 10, pp. 8231–8241, 2020.

[7] H. Nakai, K. Moriya, H. Ohtani, H. Fuma, and Y. Inaguma, "Overview of multi-functional converter systems," in *R&D Review of Toyota CRDL*, vol. 39, no. 3, pp. 27–32, 2004.

[8] K. Moriya, H. Nakai, Y. Inaguma, and S. Sasaki, "A DC/DC converter using motor neutral point and its control method," in *Proc. of National Conventional Record IEE Japan*, pp. 119–120, 2004 (in Japanese).

[9] H. Nakai, H. Ohtani, Y. Inaguma, and S. Sasaki, "Multi-functional converter systems (MFCS) using 2 neutral-points," in *Proc. of National Conventional Record IEE Japan*, pp. 289–290, 2005 (in Japanese).

[10] K. Moriya, H. Nakai, Y. Inaguma, H. Ohtani, and S. Sasaki, "A novel multi-functional converter system equipped with input voltage regulation and current ripple suppression," in *Proc. Fourtieth IAS Annual Meeting. Conf. Record of the 2005 Industry Applications Conf*, vol. 3, pp. 1636–1642 Vol. 3, 2005.

[11] J.-Y. Gauthier and X. Lin-Shi, "Voltage boost by neutral point supply of AC machine," in *Proc. ELECTRIMACS 2019, Salerno, Italy*, 2019.

[12] X. Zhang, J.-Y. Gauthier, and X. Lin-Shi, "Neutral point supply scheme for PMSM drive to boost DC voltage," in *Proc. IECON 2019 - 45th Annual Conf. of the IEEE Industrial Electronics Society*, vol. 1, pp. 3215–3220, 2019.

[13] G. T. Chiang and J. Itoh, "DC/DC boost converter functionality in a three-phase indirect matrix converter," *IEEE Trans. Power Electron.*, vol. 26, no. 5, pp. 1599–1607, 2011.

[14] H. Plesko, J. Biela, J. Luomi, and J. W. Kolar, "Novel concepts for integrating the electric drive and auxiliary dc-dc converter for hybrid vehicles," in *Proc. APEC 07 - Twenty-Second Annual IEEE Applied Power Electronics Conf. and Exposition*, pp. 1025–1031, 2007.

[15] H. Plesko, J. Biela, J. Luomi, and J. W. Kolar, "Novel concepts for integrating the electric drive and auxiliary DC-DC converter for hybrid vehicles," *IEEE Trans. Power Electron.*, vol. 23, no. 6, pp. 3025–3034, 2008.

[16] H. Plesko, J. Biela, and J. W. Kolar, "Novel modulation concepts for a drive-integrated auxiliary dc-dc converter for hybrid vehicles," in *Proc. Twenty-Fourth Annual IEEE Applied Power Electronics Conf. and Exposition*, pp. 164–170, 2009.

[17] J. Choi, H. Cha, and B. Han, "A three-phase interleaved DC-DC converter with active clamp for fuel cells," *IEEE Trans. Power Electron.*, vol. 25, no. 8, pp. 2115–2123, 2010.

[18] Q. Chen, L. Gu, Z. Lin, and G. Liu, "Extension of space-vector-signal-injection based MTPA control into SVPWM fault-tolerant operation for five-phase IPMSM," *IEEE Trans. Ind. Electron.*, vol. 67, no. 9, pp. 7321–7333, 2020.

[19] S. R. Bowes and Yen-Shin Lai, "The relationship between space-vector modulation and regular-sampled PWM," *IEEE Trans. Ind. Electron.*, vol. 44, no. 5, pp. 670–679, 1997.

[20] S. Singh and S. Sonar, "A new SVPWM technique to reduce the inductor current ripple of three-phase z-source inverter," *IEEE Trans. Ind. Electron.*, vol. 67, no. 5, pp. 3540–3550, 2020.

[21] Z. Shu, J. Tang, Y. Guo, and J. Lian, "An efficient SVPWM algorithm with low computational overhead for three-phase inverters," *IEEE Trans. Power Electron.*, vol. 22, no. 5, pp. 1797–1805, 2007.

[22] T. Hackner and J. Pforr, "Optimization of the winding arrangement to increase the leakage inductance of a synchronous machine with multi-functional converter drive," in *Proc. IEEE Energy Conversion Congress and Exposition*, pp. 1541–1548, 2011.

[23] T. Hackner, J. Pforr, H. Polinder, and J. A. Ferreira, "Optimization of the winding arrangement to increase the zero-sequence inductance of a synchronous machine with multifunctional converter drive," *IEEE Trans. Ind. Appl.*, vol. 48, no. 6, pp. 2277–2286, 2012.

Xiaokang Zhang (S'19) received the M.S. degree in electrical engineering from Northwestern Polytechnical University, Xi'an, China, in 2018. He is currently pursuing for the Ph.D. degree at the University of Lyon - Institut National des Sciences Appliquées de Lyon (INSA Lyon), Lyon, France.

His research interests include power electronics, electrical drives and fault-tolerant control techniques.

Jean-Yves Gauthier received the Ph.D. degree from the University of Franche-Comté, Besançon, France, in 2007. His Ph.D. research fields were about the modeling and the control of magnetic shape memory alloy-based actuators.

In 2008, he became an Associate Professor at the Institut National des Sciences Appliquées de Lyon (INSA Lyon), Villeurbanne, France, working on semiactive vibration control using piezoelectric devices. Since 2012, he has been working at the Ampère Laboratory, INSA Lyon. His current research interests include the control of power electronic devices and electrical motor drives.

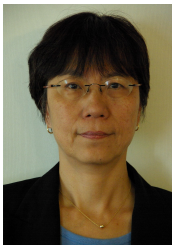

Xuefang Lin-Shi received the Ph.D. degree in applied computer science and automatic from the Institut National des Sciences Appliquées de Lyon (INSA Lyon), Villeurbanne, France, in 1992.

Since 1993, she has been with the Electrical Engineering Department, INSA Lyon, where she is currently a Professor. She is currently with the Ampère Laboratory, Lyon, France. Her research interests concern control applied to electrical drives and power electronics systems.

Romain Deploux received the M.S. degree in control system and mechatronics from the Chalmers University of Technology, Gothenburg, Sweden, in 2009 and the Ph.D. degree in control theory, data and signal processing from the École Centrale de Lille, Villeneuve-d'Ascq, France, in 2012.

In September 2014, he joined the Institut National des Sciences Appliquées de Lyon (INSA Lyon), Villeurbanne, France, and the Ampère Laboratory, where he is currently an Associate Professor. His research interests include control applications for power electronics systems, switching systems, and sliding mode control.

Jean-François Trégouët received the Ph.D. degree from Supaéro, Toulouse, France, in 2012, after performing his research at LAAS-CNRS, Toulouse. He spent several months in various research institutions such as the Politecnico di Milano, Milan, Italy, Kyoto University, Kyoto, Japan, Curtin University, Bentley, WA, Australia. He is currently an Assistant Professor with the Institut National des Sciences Appliquées de Lyon (INSA-Lyon), Villeurbanne, France. His main research interests include control design for over-actuated systems, with applications in power electronics.